Rational Design of Hierarchically-Structured Dual-Encapsulated $CoMoO_4$ Nanosheets via *in-Situ* Plasma Tuning for Efficient Li^+ Storage

Bo Ouyang [a,c,†], Ying Wang [a,†], Xi Wang [a], Zheng Zhang [b], Erjun Kan [a,*], and Rajdeep Singh Rawat [c,*]

[a] Institution of Energy and Microstructure, Department of Applied Physics, Nanjing University of Science and Technology, Nanjing 210094, China

[b] Institute of Materials Research and Engineering, A*STAR (Agency for Science, Technology and Research), #08-03, Fusionopolis Way, Innovis, 138634, Singapore

[c] Natural Sciences and Science Education, National Institute of Education, Nanyang Technological University, 637616, Singapore

[*] Email: rajdeep.rawat@nie.edu.sg, ekan@njust.edu.cn

[†] These authors contributed equally to this work

Abstract

Engineering electrode with desirable nanostructures is regarded as an urgent challenge to achieve enhanced electrical conductivity, stable structural integrity and advanced performance for Li^+ storage. Various approaches with processing complexity and multiple reactions have suffered serious limitation in industrialization. Here, we developed a facile carbon plasma (C-plasma) strategy combined with controlled reaction zone temperature to *in-situ* achieve hierarchical metallic nanoparticles and graphene encapsulated $CoMoO_4$ nanosheets (hCCO). The nano-frameworks of Co_3Mo and graphene shell are simultaneously modulated via simply controlling reaction zone temperature. The incorporation of nano-alloy component effectively enhances the conductivities of nanosheet and uniformly-coated graphene releases the structural stress caused by conversion reaction of metal oxides, maximizing the capacity utilization. The synergetic combination of these advantages enables the synthesized hCCO to have excellent electrochemical performances. Our C-plasma exhibits a great potential in tuning nano-architectures with high-performance Li^+ storage behavior.

Keywords: Carbon plasma • Dual encapsulation • Hierarchical metallic framework • Tunable carbon shell • Energy storage

1. Introduction

Poor charge transfer behaviors of transition metal oxides have restricted their efficient utilization in lithium ion storage [1, 2]. With extensive researches for decades, the encapsulation of conductive buffer materials has been regarded as a promising strategy for enhancing the Li^+ diffusion and hence the overall performance [3-5]. To date, various strategies have been adopted to coat uniform shell on the surfaces of active materials, especially using carbon and metallic coating [6-9]. In terms of the former one, the outer carbon layer, typically graphitic coating, can prevent the formation of unstable solid electrolyte interface (SEI) layer and release the mechanical stress caused by volume change of metal oxides during cycling, stabilizing the electrode structure [10, 11]. Additionally, metallic introduction, such as Ag, Co and Ni that are inert to direct reaction with Li^+, can deliver much enhanced conductivity for overall composites compared to carbon encapsulation [12-14] and thus contribute to improved efficiency due to better charge transport. However, transition metal encapsulation provides high catalytic activity in the decomposition of SEI layer. High hardness commonly causes the continuous pulverization of SEI layers, leading to rapid capacity degradation during cycling [15, 16]. Hence, an effective approach to integrate the advantages of both coatings and simultaneously prevent their inferior properties needs to be developed urgently.

Various methods have been applied to achieve dual introduction for optimizing lithium ion storage. Typically, Li et al fabricated carbon coated SiO_x-TiO_2 nanocomposites via sol-gel method [17]. TiO_2 nanoparticles were embedded inside SiO_x, improving the overall conductivity and maintaining the structural integrity. Meanwhile, the carbon shell minimized the side reactions of the active materials with the electrolyte, ensuring fast reaction kinetics. Sun et al fabricated Co/CoO_x nanoparticles anchored porous carbon cuboid based on the carbonization of polymer followed by metallic impregnation [12]. The outstanding electrochemical performance was attributed to the increased conductivity of metallic cobalt nanoparticles and enhanced active surface area of porous carbon with numerous defects. Although above researches have delivered nano-composites with excellent Li^+ storage properties, most approaches had to introduce environmentally-hazardous species and long-term annealing with multi-reaction steps, restricting the scalable application in lithium ion batteries (LIBs) [18, 19]. Additionally, the high temperature during thermal treatment inevitably causes the nanostructure agglomeration, which makes it quite difficult to precisely modulate the morphologies and structures of nano-composites. Thereby, a simple and fast technique is required for the controllable fabrication of nano-composites with high-performance Li^+ storage behavior.

Here, we applied a facile C-plasma strategy for the controllable fabrication of dual-encapsulated $CoMoO_4$ nanosheets. After rapid C-plasma treatment (30 s), hierarchically decorated Co_3Mo nanoparticles and uniform graphene shell are simultaneously grown on nanosheet surfaces. The optimized alloy nano-frameworks along

with highly-crystalized graphene at moderate temperature of 450 ºC contributes to great conductivity and structural accommodation, leading to excellent lithium ion storage behavior, while lower or excessive processing temperature cause the amorphous carbon deposition or metallic nano-assembly formation, respectively, resulting in the structural pulverization with limited capability. The *in-situ* achieved nanoparticles provides enhanced electronic and lithium ionic conductivities and meanwhile, graphene shell deliver great structural preservation, leading to excellent Li^+ storage behavior, with high specific capacity (770 mA h g^{-1} at 0.4 A g^{-1}) and great cyclability (641 mA h g^{-1} at 1.6 A g^{-1} for 1000 cycles). Our C-plasma technique, hence, unveils a novel and simple pathway in tuning nano-architectures for high-performance energy storage materials.

2. Results and Discussion

The schematic of the fabrication process of hierarchical nano-frameworks based on C-plasma strategy is illustrated in Fig. 1. $CoMoO_4$ nanosheets (CMO) were uniformly grown on the surface of Ni foam via hydrothermal approach. The surface morphology and deposited carbon nanostructure were simultaneously modulated by simply controlling reaction temperature, indicating the efficiency of *in-situ* tuning via C-plasma processing. Upon plasma processing with suitably tailored reaction temperature, metallic nano-particles with different amounts and diameters are hierarchically grown on nanosheet surfaces along with the uniform encapsulation by different carbon shells, resulting from the carbothermal reduction and surface deposition of plasma [20, 21]. With the processing temperature ≤150 ºC, amorphous carbon shell is observed on CMO nanosheet surfaces with relatively low Co_3Mo formation. The raise in reaction zone temperature to 250-350 ºC, resulted in separately distributed alloy nanoparticles on sheet surfaces with graphitic carbon shell. Further increase in temperature to 350-450 ºC lead to the dense distribution of metallic nanoparticles and graphene encapsulation with less defects. Excessive reaction temperature above 550 ºC caused the agglomeration of nanoparticles and superfluous graphene deposition, leading to the partial pulverization of nano-framework. Compared with conventional processes, our C-plasma with controlled plasma temperature can easily modulate the hierarchical Co_3Mo nano-structures and simultaneously achieve uniform carbon shell. Additionally, such strategy requires much lower temperature (≤550 ºC) and C-plasma processing duration (≤30 s), resulting in preservation of nanosheet structures and rationally tailored 3D macro-porous network. These hierarchical nano-morphologies were attributed to the synergistic effect of active C-species and reaction temperature.

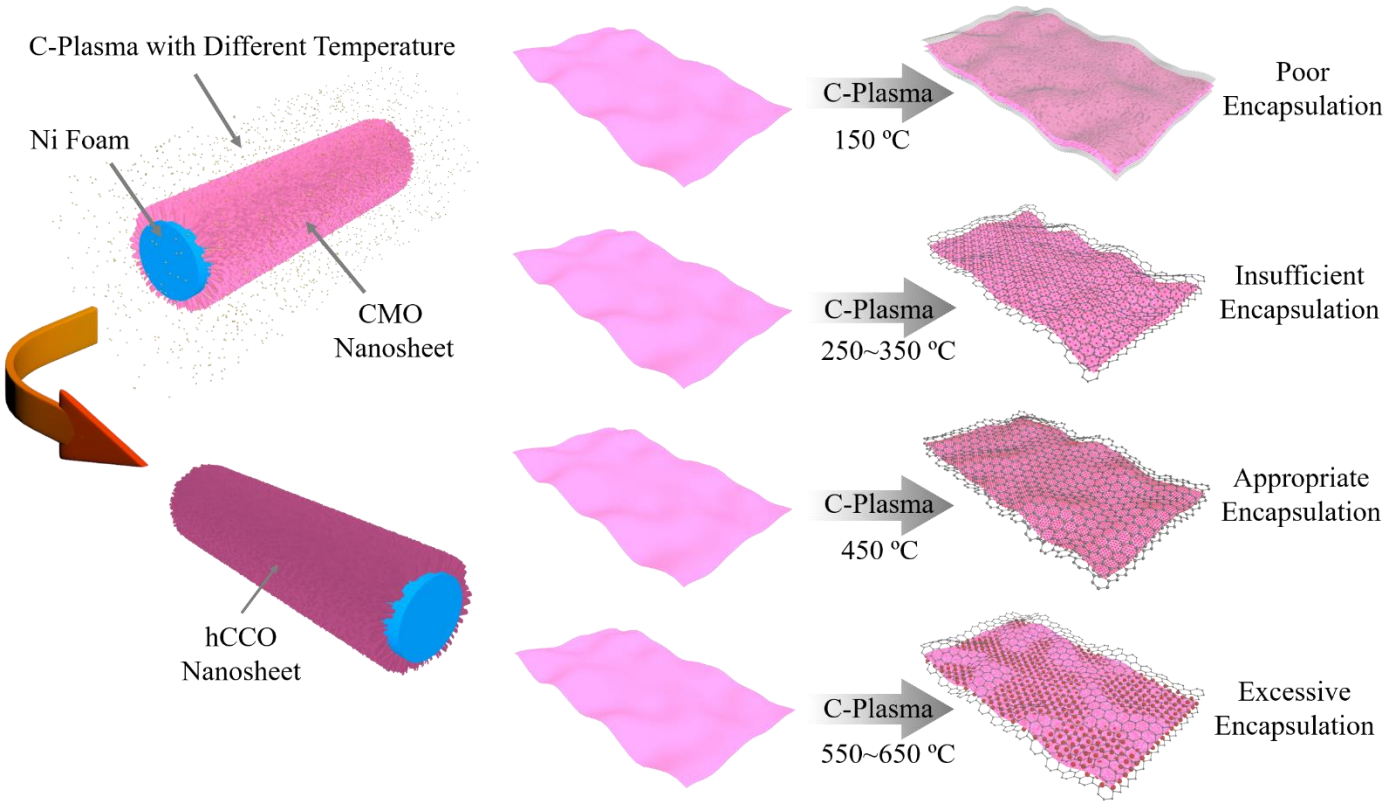

Fig. 1. The fabrication procedure of hCCO nanosheets via C-plasma and schematic illustration of the achieved nanosheets with different surface modulation based on different processing temperature.

Detailed scanning electron microscopy (SEM) characterizations are carried out to determine the surface morphology of as-prepared nano-composites. As shown in Fig. 2a, initial CMO sample shows vertically-oriented nanosheet arrays with smooth surfaces. With reaction temperature of 150 ºC (Fig. 2b), separated nano-assemblies with the diameter of 40 nm are deposited on nanosheet surfaces with the clear increase of nanosheet thickness, which suggests the amorphous carbon deposition due to low-energy C-species in plasma environment. With temperature rising to 250 ºC (Fig. 2c), the increased number of metallic nanoparticles with similar sizes was formed along with large amounts of carbon nano-assemblies deposited on nanosheet surfaces, which was derived from the activated C-species in plasma. C-species also caused the independent formation of amorphous carbon assembly, leading to the adsorption of numerous carbon-assemblies on nanosheet surfaces and edges. Such phenomenon was common in terms of plasma deposition [22, 23]. The C-plasma treatment at 350 ºC (Fig. 2d) resulted in nanosheet thickness similar to the C250 with much reduced number of carbon nano-assemblies. This is due to the presence of more active carbon species with raised energy, leading to the reduced formation of amorphous carbon and increased metallic Co_3Mo achievement. Further increase in reaction temperature to 450 ºC caused the optimized hierarchical nanostructures (Fig. 2e) with the smallest cobalt nanoparticles and the minimized amorphous carbon deposition, leading to the enhanced Li^+ storage performance. Additionally, C550 sample with C-plasma treatment at 550 ºC (Fig. 2f) led to the tremendous reduction of oxide nanosheets and even partial pulverization of nanosheets owing to the

significantly increased energy of carbon species, and extremely-energetic carbon species caused the total pulverization of nanosheets during processing at 650 ºC (Fig. S1).

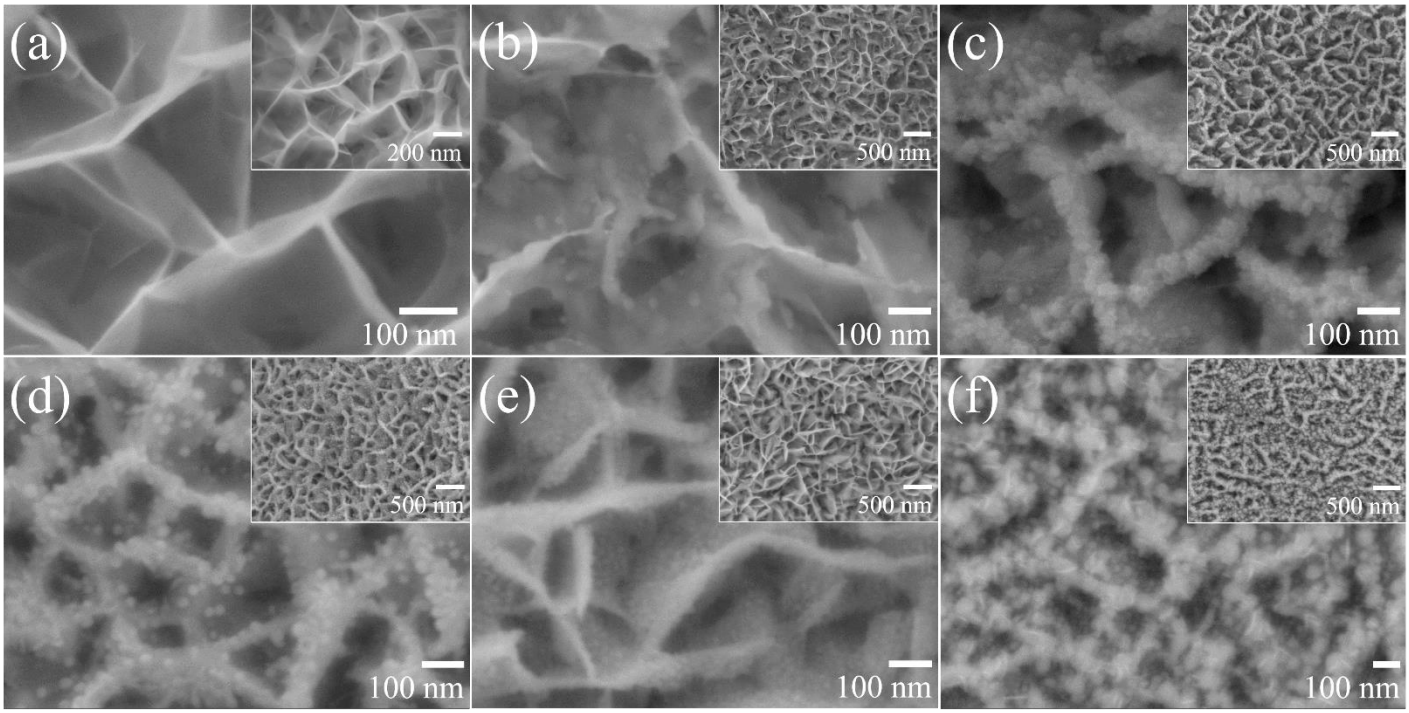

Fig. 2. The schematic diagram of achieved hCCO with different surface morphologies with C-plasma processing at different reaction temperature. (a) initial, (b) 150 ºC, (c) 250 ºC, (d) 350 ºC, (e) 450 ºC, (f) 550 ºC.

The transmission electron microscopy (TEM) is conducted to investigate the finer morphological, structural and elemental composition of the resultant composites before and after the C-plasma treatment. Fig. 3a exhibits the smooth nanosheet structure of initial CMO. The lattice fringes with *d*-spacing of 0.24 nm can be clearly distinguished, corresponding to (-222) plane of $CoMoO_4$ (Fig. 3b) [24]. The uniform distributions of Co, Mo and O signals in nanosheets with atomic ratio of 1:1:4 are further confirmed by elemental mapping in the scanning transmission electron microscopy (STEM) images, confirming the presence of $CoMoO_4$ (Fig. 3c). Plasma treatment at 150 ºC causes the deposition of amorphous carbon on nanosheet surfaces with little metallic nanoparticle formation, which is ascribed to insufficient energy of C-species (Fig. S2). As the reaction temperature increases to 250 ºC, the graphitic carbon encapsulation and numerous nanocrystals are simultaneously achieved on the surface of nanosheets (Fig. 3d). Further observations verify the lattice spacing of 0.34 nm in (002) plane of graphene and a spacing of 0.24 nm in (-222) plane of $CoMoO_4$, indicating excellent structural preservation (Fig. 3e). As shown in elemental mapping (Fig. 3f), the uniform distribution of C signal is observed, indicating the full encapsulation by graphitic carbon. After plasma treatment at 350 ºC (Fig. S3a), numerous nanoparticles with mean diameters of 4 nm are hierarchically dispersed on the sheet surface along with well-defined graphene shell. The lattice spacing of 0.19 nm is provided in these nanoparticles, corresponding to the (202) plane of Co_3Mo alloy (Fig. S3b) [25]. In addition, elemental maps

apparently exhibit the enrichment Co signal at the position of metallic particles, which elucidates the successful formation of hierarchical nanoalloy (Fig. S3c). Further raised temperature at 450 ºC leads to the similar results, simultaneously delivering hierarchical Co_3Mo nanoparticles and multi-layer graphene grown on nanosheets (Fig. 3g and 3h). STEM and mapping show the same phenomenon with C350 sample, confirming the achievement of alloy particles on nanosheet surface (Fig. 3i). Processing at excessive temperature of 550 ºC results in the aggregation of metallic nano-assemblies with the diameter of 20 nm, which inevitably causes partial nanosheet pulverization and hence limits the Li^+ storage behavior (Fig. S3d-S3f) [26, 27].

In addition, Raman spectroscopy, X-ray diffraction (XRD) and X-ray photoelectron spectroscopy (XPS) are conducted to confirm the crystal structures and chemical bonding in the resultant nano-composites. As shown in Raman spectra (Fig. 4a and S4), initial CMO nanosheets provide peaks below 1000 cm^{-1}, ascribed to the specific bands of metal oxides. After C-plasma treatment, two peaks at 1345 and 1558 cm^{-1} are observed, which are attributed to D and G bands of carbon shell [28]. With increase in processing temperature, the intensities of D and G peaks enhanced along with the disappearance of oxide-based peaks, elucidating the full encapsulation of carbon shell and the reduction of oxides. Additionally, raised reaction temperatures cause the transition of two carbon peaks from highly overlap-type to reasonably well-segregated state with increased sharpness, which indicates the conversion from amorphous to graphitic carbon shell as well as the reduced deposition of amorphous carbon assembly on nanosheet surfaces. Noticeably, 2D band at 2640 cm^{-1} is apparently observed in hCCO and C550 but absent in other samples, suggesting the formation of highly crystalized graphene layer with less-disordered carbon. In terms of XRD patterns (Fig. 4b), bare CMO provides well-defined (021), (002), (222), (112) and (023) planes, and achieved Co_3Mo phase via C-plasma processing delivers (002) and (202) planes, which demonstrates the successful *in-situ* growth of hierarchical Co_3Mo nanoparticles [25, 29]. The XPS survey spectra are given in Fig. 4c, in which C-binding intensities continually enhance with raised reaction temperature, opposite to that of O-binding. This confirms the oxygen removal via carbon species and the reduction of metal oxides, accompanying with the formation of carbon layer. As depicted in Co 2p spectra (Fig. 4d), Co-O bands at 781.9 and 787.0 eV are present in all samples, while metallic Co band, at 778.7 eV, is only observed in C250 and hCCO composites, confirming the formation of metal species after plasma treatments. According to Mo 3d spectra (Fig. 4e), the CMO nanosheets show the Mo-O bonding at 232.7 and 235.8 eV, validating the Mo $3d^5$ and Mo $3d^3$ peaks of MoO_3. Upon plasma processing, two new binding energy peaks corresponding to MoO_2 and metallic Mo appear at 232.2 and 229 eV, respectively, which elucidates the carbothermal reduction in heated C-plasma environment [30]. Correspondingly, enhanced peak intensities of metallic Co and Mo is adherent with raised temperature from

250 to 450 ºC, which confirms the increased amounts of reduced metals. In addition, C250 sample provides apparent peak at 285 eV, attributed to C-C binding of amorphous carbon, while C-C bond at 284.5 eV serves as the major components in hCCO, elucidating the deposition of graphitic carbon (Fig. 4f). The small peak at 286.4 eV, in both samples, is associated with C-O bond, which is related to a common phenomenon of oxygen introduction during carbon formation [31]. Comparatively, initial CMO nanosheet deliver little carbon-based peak, inducing no impurity on its surface.

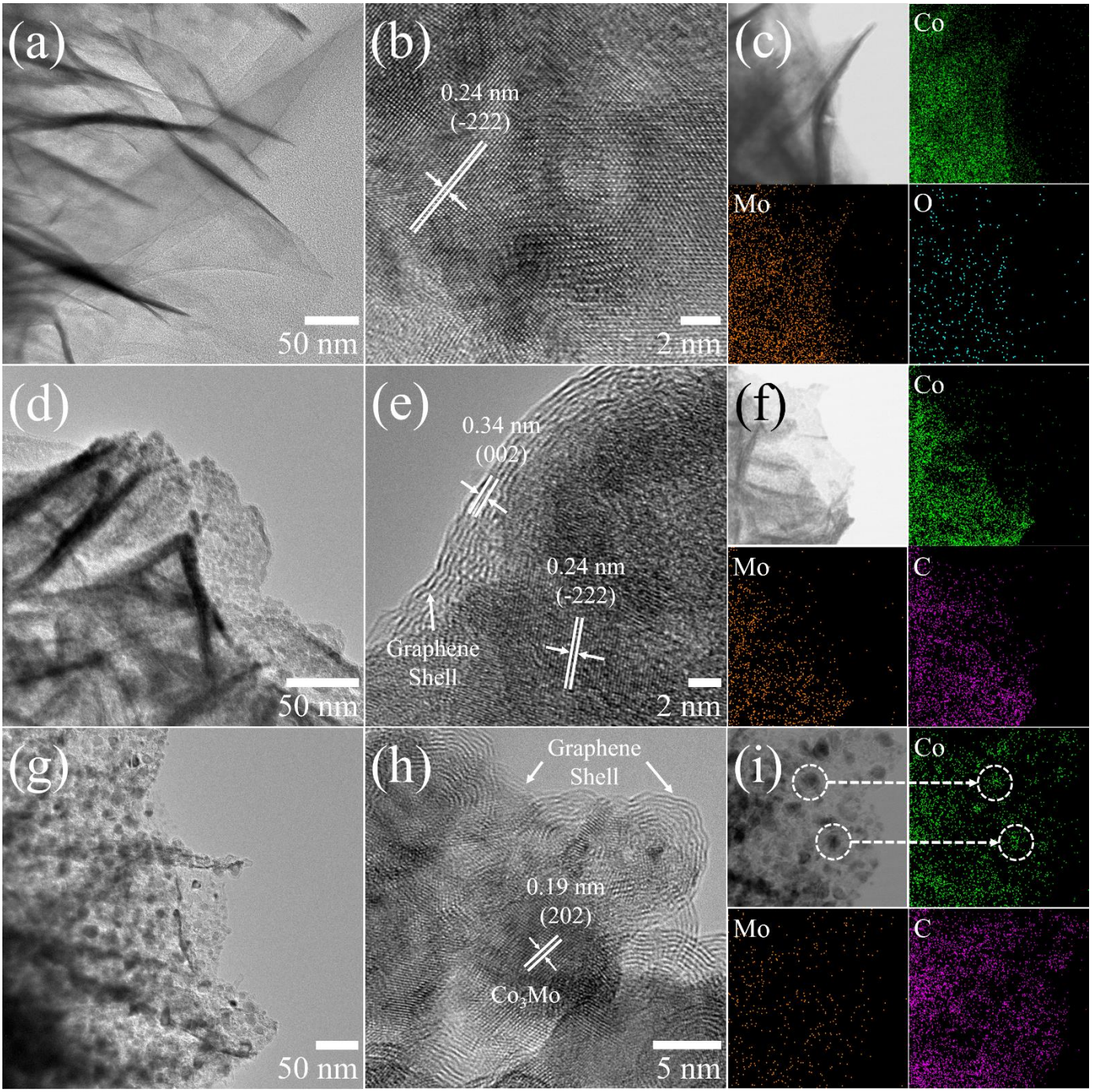

Fig. 3. The TEM observation and corresponding elemental mapping of CMO, C250 and hCCO composites. (a-c) CMO, (d-f) C250, (g-i) hCCO.

With the above elaborate characterizations, it is confidently concluded that hCCO nano-composites have

been successfully fabricated via our facile approach. As confirmed, C-plasma can rapidly achieve hierarchical metallic nano-particles and simultaneously the carbon shell on nanosheet surfaces. The diameters of metallic Co_3Mo nanoparticles and the type of carbon encapsulation can be easily modulated via simply controlling reaction temperature from 150 to 650 ºC during C-plasma processing. In terms of Li^+ storage property, the achieved metallic nano-particles improve the charge transport behavior of nanosheets, and carbon shell contribute to the stable SEI layer, predicting a favorable electrode material. In terms of our nano-composites, plasma-produced C-species at lower reaction temperature causes the deposition of amorphous carbon with little metal growth, while high temperature leads to multi-layer graphene formation with agglomeration of reduced alloy, which inevitably restricts the overall electrochemical performances. We hypothesize that the electrode materials with appropriate nano-alloy and highly-crystallized graphene layer, obtained by C-plasma processing at moderate reaction temperature, is going to provide excellent LIB performance.

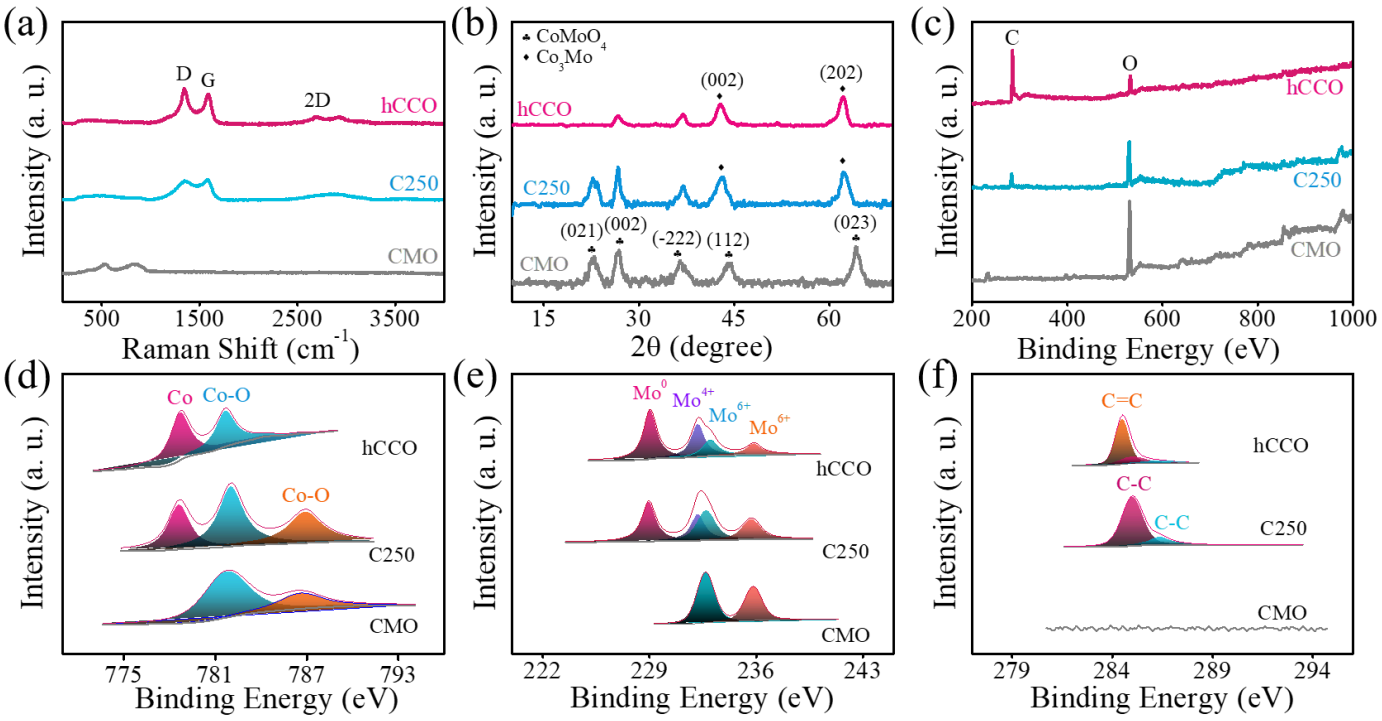

Fig. 4. The characterizations of CMO, C250 and hCCO composites. (a) Raman spectra, (b) XRD pattern, (c) XPS spectra, XPS high resolution spectra of (d) Co 2p, (e) Mo 3d, (f) C 1s.

To verify our hypothesis, we apply the bare CMO, C250 and hCCO as the LIB anodes for electrochemical property evaluation. Fig. 5a exhibits the cyclic voltammetry (CV) curves of hCCO. In the initial cathodic process, the well-defined peak at 1.42 V can be attributed to the conversion reaction of active materials with Li^+, followed by the preliminary decomposition of electrolyte and some irreversible reactions at 0.22 V. In comparison, CMO and C250 anodes exhibit the distinct peak below 0.5 V with increased intensity (Fig. S6), suggesting more irreversible reaction during the initial discharging process. Meanwhile, the other peak in CMO and C250 anodes exhibits much weaker intensity than that of hCCO, further inferring its enhanced

reversible reaction. During the 1st anodic process, the broad peaks at 1.50 and 2.33 V are observed in these electrodes, corresponding to the delithiation of metal oxides [32]. For hCCO and C250, the CV curves overlap well during the subsequent cycling, confirming great reversibility for the redox reaction, in stark comparison to that of CMO electrode. The galvanostatic charge-discharge (GCD) profiles are further examined, in which the multiple plateaus during the initial discharging and charging processes demonstrate multi-reactions (Fig. 5b). Typically, a plateau between 1.0 and 1.4 V indicates the redox reaction of metal oxide with Li^+, in which hCCO provides the highest reversible capacity, followed by C250 and CMO electrodes. This is consistent with CV results. Moreover, the hCCO exhibits initial discharge capacity of 1089 mA h g^{-1} than that of C250 (1010 mA h g^{-1}) and CMO (892 mA h g^{-1}). The corresponding Columbic efficiencies are 64% for hCCO, 61% for C250 and 54% for CMO electrodes. The reason for enhanced reversible capacity of hCCO can be explained by the improved charge transport behavior and graphene shell to preserve SEI layer.

The rate capabilities of these samples are compared in Fig. 5c, in which all samples were cycled under current densities from 0.4 to 3.2 A g^{-1}. The average capacities of 770, 620, 503 and 384 mA h g^{-1} at rates of 0.4, 0.8, 1.6, 3.2 A g^{-1} can be achieved in hCCO anode, which are much higher than those of C250 (693, 558, 406, 272 mA h g^{-1}) and CMO (590, 479, 343, 217 mA h g^{-1}). Even at a rate as high as 3.2 A g^{-1}, a reversible capacity of 384 mA h g^{-1} for hCCO can be preserved, still higher than that of commercial graphite at low current density. It is worth noting that a specific capacity of 674 mA h g^{-1} can be restored and maintained for 150 cycles with little capacity fading when the current density returns to 0.4 A g^{-1}, 97.3% of the capacity recovery. By contrast, C250 delivers continuous capacity fading when the current rate is switched back to 0.4 A g^{-1}, with 62% capacity retention after 150 cycling. The initial CMO electrode exhibits a rapid capacity fading. The above results suggest the outstanding rate performance and excellent recovery capacity of hCCO materials. The positive effects of dual-encapsulation on the reaction kinetics of hCCO electrode can be understood from the electrochemical impedance spectroscopy (EIS) results. As observed in Fig. 5d, the hCCO electrode exhibits much smaller semicircle than that of C250 and CMO, indicating the lower charge transfer resistance (R_{ct}) and fast reaction kinetics of such hierarchical nano-framework.

The long-term cyclability of hCCO, C250 and CMO electrodes is further evaluated at the current density of 1.6 A g^{-1} (Fig. 6a). After 1000 cycles, the hCCO electrode exhibits a stable reversible capacity of 641 mA h g^{-1} without any degradation, demonstrating its outstanding long-term cyclability at high rate condition. Noticeably, its specific capacity during cycling is firstly reduced followed by a gradual increase with retention above 100%, which is related to the catalytic effect of Co_3Mo alloy to reduce Li_2O and the re-generation of metal oxides [13]. Meanwhile, the metallic nanoparticles in hCCO are capable of improving the accessibility of Li^+ to storage sites and the graphene shell promotes structural stability of the composites, leading to the

exceptional electrochemical performance of hCCO. On the contrary, C250 electrode provide capacity of 205 mA h g^{-1} after 1000 cycles with retention of 55%, which may be associated with the low electronic conductivity of nano-composites and structural instability of amorphous carbon encapsulation. Bare CMO sample delivers rapid capacity decay during the first 200 cycles and retained negligible performance. Such excellent specific capacity, rate behavior and cycling performance of our nano-frameworks are comparable or even superior to those of state-of-the-art CMO-based anodes in previous studies (Table S1).

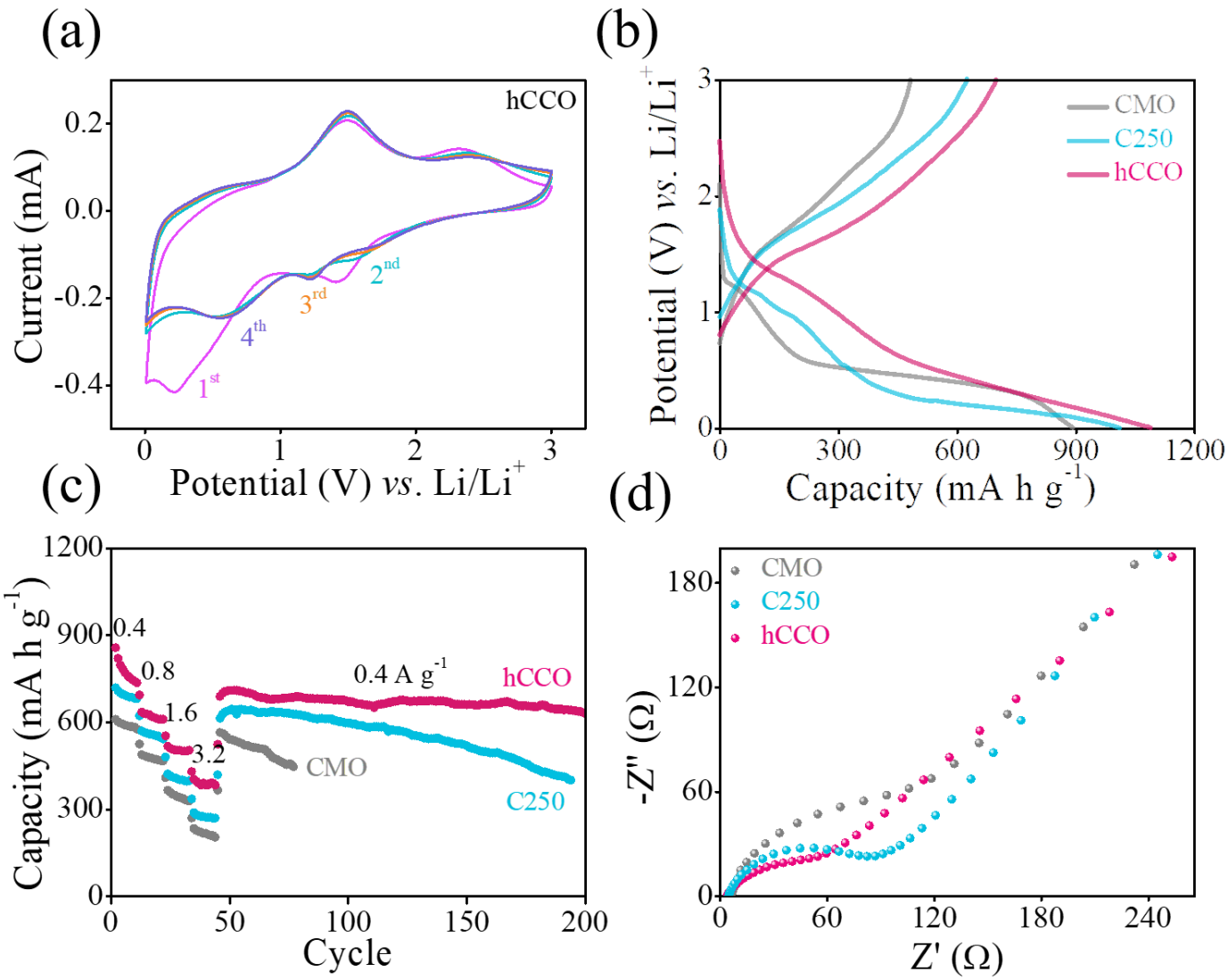

Fig. 5. Electrochemical performance and kinetics of CMO, C250 and hCCO. (a) initial CV curves of the hCCO, (b) initial GCD profiles at 0.4 A g^{-1}, (c) the comparison of rate capabilities, (d) the comparison of EIS spectra.

To comprehend the Li^+ storage process of hCCO, C250 and CMO electrodes, the apparent diffusion coefficient of lithium ions (D_{Li^+}) and the ratio of pseudocapacitive contribution are analyzed based on galvanostatic intermittent titration technique (GITT) and CV tests. According to Fig. 6b and S7, the D_{Li^+} of three electrodes during discharging and charging processes are calculated based on Fick's second diffusion law as below:

$$D_{Li^+} = \frac{4}{\pi\tau}\left(\frac{m_B V_M}{M_B S}\right)^2 \left(\frac{\Delta E_S}{\Delta E_\tau}\right)^2$$

Where τ, m_B, M_B, V_M, S stand for the pulse duration, mass, molar mass and molar volume of active materials, respectively. ΔE_S and ΔE_τ are obtained from the GITT curves (Fig. S7) [33]. The diffusion coefficient, D_{Li^+}, of three electrodes during discharging process are plotted in Fig. 6b as a function of applied potential. The coefficient increases rapidly from 0.4×10^{-12} to 0.8×10^{-12} cm^2 s^{-1} for hCCO followed by a distinct plateau between 0.2 and 0.7 V, which indicates hierarchical metal nanoparticles to facilitate Li^+ diffusion and achieve large D_{Li^+} in the plateau region. A sudden drop of the coefficient below 0.2 V is ascribed to the process that Li^+ overcomes the resistance derived from previously existing lithium ions to insert into active materials. This indicates that hierarchical alloy nanoparticles with graphene encapsulation allow for rapid transfer of electrons and ions. Comparatively, C250 provides much reduced diffusion coefficient in the range between 0.2×10^{-12} and 0.03×10^{-12} cm^2 s^{-1} along with negligible D_{Li^+} below 1.0×10^{-15} cm^2 s^{-1}. This is originated from decreased amounts of metallic nanostructures and amorphous carbon shell, leading to reduced charge transfer behavior. Additionally, the coefficients of all samples during charging process also display similar trends (Fig. S8), further validating much enhanced Li^+ transport behavior in hCCO nano-structures.

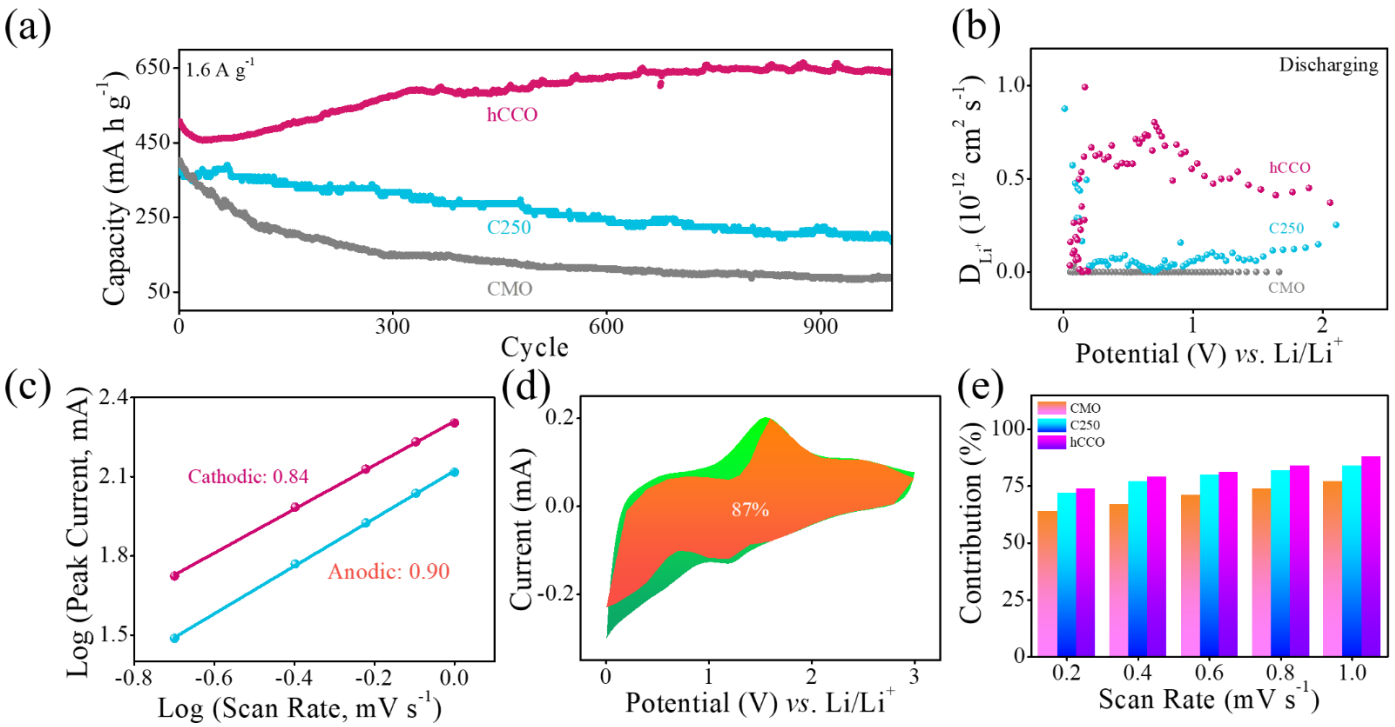

Fig. 6. Cycling stability and charge storage mechanism of CMO, C250 and hCCO. (a) the comparison of long-term cycling behaviors at 1.6 A g^{-1}, (b) the comparison of calculated diffusion coefficients during discharging process, (c) plot of log (scan rate) versus log (peak current), (d) pseudocapacitive contribution of hCCO at 1.0 mV s-1, (e) the pseudocapacitive contribution comparison at different scan rates.

The level of capacitive contribution is further qualitatively analyzed by plotting the log (scan rate)-log (peak current) curves. The CV curves of these electrodes at scan rates from 0.2 to 1.0 mV s^{-1} are exhibited in Fig. S9. Based on Equation $i = av^b$, the value of b can be determined from the slope of the log i versus log v curve, which can be ascribed to the diffusion-controlled process (b = 0.5) and pseudocapacitive-controlled behavior (b = 1.0) [34]. As calculated, the b is 0.84 and 0.90 for hCCO during cathodic and anodic processes along with that above 0.5 for C250 and CMO, which demonstrates the essential pseudocapacitive contribution of these electrodes (Fig. 6c and S10). The proportion of capacitive contribution can be further quantified based on $i(V) = k_1 v + k_2 v^{1/2}$, in which $k_1 v$ and $k_2 v^{1/2}$ terms refer to the surface capacitive behavior and the diffusion-controlled process, respectively. By confirming k_1 and k_2, the fraction of pseudocapacitive contribution at different scan rates can be quantified. As exhibited in Fig. 6d, 88% of total capacity for hCCO can be attributed to the capacitive contribution at 1.0 mV s^{-1}, while pseudocapacitive behaviors contributes 84% and 78% of total capabilities in C250 and CMO electrodes. Furthermore, such contribution is compared at different current densities (Fig. 6e), in which hCCO provides capacitive contribution of 74% and 84% at 0.4 and 0.8 mV s^{-1} respectively, higher than those of C250 (77 and 82%) and CMO (67 and 74%). The high ratio of capacitive behavior in hCCO at high current densities is beneficial for the rate performance, which unveils that hCCO electrode presents a better rate stability than C250 and CMO electrodes.

3. Conclusion

In summary, we have developed a facile C-plasma strategy in fabricating hierarchical Co_3Mo nanoparticles anchored $CoMoO_4$ nanosheet with graphene encapsulation for high-performance electrode in lithium ion storage. By simply controlling reaction temperature, the amounts and diameters of dispersed alloy nano-frameworks along with uniformly coated carbon shell can be simultaneously modulated to achieve the enhanced electrochemical performance. Insufficient temperature causes the deposition of numerous amorphous carbons with metallic nanoparticles owing to low-energetic carbon species, while excessive temperature leads to the structural pulverization of nano-composites due to metallic agglomeration. With the appropriate reaction condition, the graphene encapsulated nanosheets with hierarchically distributed metallic nanoparticles is achieved with enhanced Li^+ transport behavior, and hence excellent capability. High-crystallized graphitic carbon shell can further accommodate the volume changes during long-term cycling, resulting in excellent cyclability. Our C-plasma processing at moderate reaction temperature provides a novel and simple approach in tuning nano-composites for high-performance LIB electrodes.

Declaration of competing interest

The authors declare that they have no known competing financial interests or personal relationships that could have appeared to influence the work reported in this paper.

Acknowledgement

This study at Nanjing University of Science and Technology is supported by the NSFC (51522206, 11774173, 11574151, 51790492), by the Fundamental Research Funds for the Central Universities (No.30915011203, No.30918011334), China, and was also supported by IAEA, Vienna, Austria, Research Contract 22770 (CRP Code F13019) and NIE RS-SAA grant RS 6/18 RSR provided by National Institute of Education, Nanyang Technological University, Singapore.

References

[1] M.-S. Balogun, Y. Luo, W. Qiu, P. Liu, Y. Tong, Carbon 98 (2016) 162-178.

[2] Y. Zhao, L.P. Wang, M.T. Sougrati, Z. Feng, Y. Leconte, A. Fisher, M. Srinivasan, Z. Xu, Adv. Energy Mater. 7 (2017) 1601424.

[3] Y. Wen, Y. Zhu, A. Langrock, A. Manivannan, S.H. Ehrman, C. Wang, Small 9 (2013) 2810-2816.

[4] R. Mo, D. Rooney, K. Sun, H.Y. Yang, Nature Commun. 8 (2017) 13949.

[5] J. Ji, H. Ji, L.L. Zhang, X. Zhao, X. Bai, X. Fan, F. Zhang, R.S. Ruoff, Adv. Mater. 25 (2013) 4673-4677.

[6] C. He, S. Wu, N. Zhao, C. Shi, E. Liu, J. Li, ACS Nano 7 (2013) 4459-4469.

[7] C. Zhang, H. Song, C. Liu, Y. Liu, C. Zhang, X. Nan, G. Cao, Adv. Funct. Mater. 25 (2015) 3497-3504.

[8] N. Mahmood, C. Zhang, F. Liu, J. Zhu, Y. Hou, ACS Nano 7 (2013) 10307-10318.

[9] C. Tang, Y. Liu, C. Xu, J. Zhu, X. Wei, L. Zhou, L. He, W. Yang, L. Mai, Adv. Funct. Mater. 28 (2018) 1704561.

[10] J. Chang, X. Huang, G. Zhou, S. Cui, P.B. Hallac, J. Jiang, P.T. Hurley, J. Chen, Adv. Mater. 26 (2014) 758-764.

[11] L. Shi, C. Pang, S. Chen, M. Wang, K. Wang, Z. Tan, P. Gao, J. Ren, Y. Huang, H. Peng, Z. Liu, Nano Lett. 17 (2017) 3681-3687.

[12] X. Sun, G.-P. Hao, X. Lu, L. Xi, B. Liu, W. Si, C. Ma, Q. Liu, Q. Zhang, S. Kaskel, O.G. Schmidt, J. Mater. Chem. A 4 (2016) 10166-10173.

[13] C. Kim, J.-W. Jung, K.R. Yoon, D.-Y. Youn, S. Park, I.-D. Kim, ACS Nano 10 (2016) 11317-11326.

[14] F. Zou, Y.-M. Chen, K. Liu, Z. Yu, W. Liang, S.M. Bhaway, M. Gao, Y. Zhu, ACS Nano 10 (2016) 377-386.

[15] S. Solchenbach, G. Hong, A.T.S. Freiberg, R. Jung, H.A. Gasteiger, J. Electrochem. Soc. 165 (2018) A3304-A3312.

[16] T. Kim, L.K. Ono, N. Fleck, S.R. Raga, Y. Qi, J. Mater. Chem. A 6 (2018) 14449-14463.

[17] Z. Li, H. Zhao, P. Lv, Z. Zhang, Y. Zhang, Z. Du, Y. Teng, L. Zhao, Z. Zhu, Adv. Funct. Mater. 28 (2018) 1605711.

[18] Y. Chen, X. Li, X. Zhou, H. Yao, H. Huang, Y.-W. Mai, L. Zhou, Energy Environ. Sci. 7 (2014) 2689-

2696.

[19] C. Yang, Y. Yao, S. He, H. Xie, E. Hitz, L. Hu, Adv. Mater. 29 (2017) 1702714.

[20] B. Ouyang, D. Chao, G. Jia, Z. Zhang, H.J. Fan, R.S. Rawat, Energy Storage Mater. 18 (2019) 462-469.

[21] D. Chao, B. Ouyang, P. Liang, T.T.T. Huong, G. Jia, H. Huang, X. Xia, R.S. Rawat, H.J. Fan, Adv. Mater. 30 (2018) 1804833.

[22] N. Bundaleska, D. Tsyganov, A. Dias, E. Felizardo, J. Henriques, F.M. Dias, M. Abrashev, J. Kissovski, E. Tatarova, Phys. Chem. Chem. Phys. 20 (2018) 13810-13824.

[23] V.I. Merkulov, A.V. Melechko, M.A. Guillorn, D.H. Lowndes, M.L. Simpson, Appl. Phys. Lett. 79 (2001) 2970-2972.

[24] Y. Zhang, C. Liu, X. Gao, Z. Luo, J. Hu, G. Zou, H. Hou, Z. Xu, X. Ji, Nano Energy 68 (2020) 104333.

[25] E.V. Lobiak, E.V. Shlyakhova, L.G. Bulusheva, P.E. Plyusnin, Y.V. Shubin, A.V. Okotrub, J. Alloy Compds 621 (2015) 351-356.

[26] C. Gao, Z. Jiang, P. Wang, L.R. Jensen, Y. Zhang, Y. Yue, Nano Energy 74 (2020) 104868.

[27] D. Ma, Y. Li, H. Mi, S. Luo, P. Zhang, Z. Lin, J. Li, H. Zhang, Angew. Chem. Int. Ed. 57 (2018) 8901-8905.

[28] B. Ouyang, D. Chao, G. Jia, Z. Zhang, E. Kan, H.J. Fan, R.S. Rawat, Nano Energy 80 (2021) 105557.

[29] J. Wang, X. Zhang, Q. Wei, H. Lv, Y. Tian, Z. Tong, X. Liu, J. Hao, H. Qu, J. Zhao, Y. Li, L. Mai, Nano Energy 19 (2016) 222-233.

[30] Y. Zhang, B. Ouyang, K. Xu, X. Xia, Z. Zhang, R.S. Rawat, H.J. Fan, Small 14 (2018) 1800340.

[31] B. Ouyang, Y. Wang, Z. Zhang, R.S. Rawat, Electrochim. Acta 194 (2016) 151-160.

[32] Y. Chen, B. Liu, W. Jiang, Q. Liu, J. Liu, J. Wang, H. Zhang, X. Jing, J. Power Sources 300 (2015) 132-138.

[33] D.W. Dees, S. Kawauchi, D.P. Abraham, J. Prakash, J. Power Sources 189 (2009) 263-268.

[34] Y. Son, J. Ma, N. Kim, T. Lee, Y. Lee, J. Sung, S.-H. Choi, G. Nam, H. Cho, Y. Yoo, J. Cho, Adv. Energy Mater. 9 (2019) 1803480.